Guthrie, Andrew; Satrya, Christoforus Dimas; Chang, Yu Cheng; Menczel, Paul; Nori, Franco; Pekola, Jukka P.

Cooper-Pair Box Coupled to Two Resonators

Cooper-Pair Box Coupled to Two Resonators: An Architecture for a Quantum Refrigerator

Andrew Guthrie⊙,[1,*] Christoforus Dimas Satrya⊙,[1,†] Yu-Cheng Chang⊙,[1] Paul Menczel⊙,[2] Franco Nori⊙,[2,3] and Jukka P. Pekola[1,4]

[1] *Pico group, QTF Centre of Excellence, Department of Applied Physics, Aalto University School of Science, P.O. Box 13500, Aalto 00076, Finland*
[2] *Theoretical Physics Laboratory, RIKEN Cluster for Pioneering Research, Wako-shi, Saitama 351-0198, Japan*
[3] *Department of Physics, The University of Michigan, Ann Arbor, Michigan 48109, USA*
[4] *Moscow Institute of Physics and Technology, Dolgoprudny 141700, Russia*

Superconducting circuits present a promising platform with which to realize a quantum refrigerator. Motivated by this, we fabricate and perform spectroscopy of a gated Cooper-pair box, capacitively coupled to two superconducting coplanar-waveguide resonators with different frequencies. We experimentally demonstrate the strong coupling of a charge qubit to two superconducting resonators, with the ability to perform voltage driving of the qubit at gigahertz frequencies. We go on to discuss how the measured device could be modified to operate as a cyclic quantum refrigerator by terminating the resonators with normal-metal resistors acting as heat baths.

I. INTRODUCTION

The study of quantum heat engines and refrigerators plays a key role in the investigation of the fundamental relationship between quantum mechanics and thermodynamics [1–4]. However, experimental realizations of cyclic quantum thermal engines have remained elusive. Such systems, in their most basic form, consist of a working substance with quantized energy levels that can be selectively coupled to a series of thermal reservoirs and are capable of transporting heat [5]. By modulation of the working-substance energy-level separation, for example, the system can be tuned to interact with each thermal reservoir sequentially. Moreover, by periodic modulation of the system energy levels, a quantum heat engine or quantum refrigerator can be actualized [6,7].

A multitude of platforms have been proposed and explored to realize quantum thermal machines. In a seminal paper [8], an ion held in a linear Pauli trap has been used to extract work by alternate exposure between a white-noise electric field (hot reservoir) and a laser cooling beam (cold reservoir). More recently, a solid-state quantum dot has been operated as a "particle exchange" heat engine, where the dot can control a thermally driven flow of charge carriers [9]. In a further development, a ^{13}C nuclear spin has been utilized to implement an Otto cycle

using a nuclear-magnetic-resonance setup [10]. Additionally, an electron-spin impurity has been shown to act as an analog heat engine, with the "thermal" reservoirs inferred by the relative chemical potential in the leads [11]. However, in all such systems, the heat current cannot be probed directly and must be inferred from an additional parameter.

Circuit quantum electrodynamics (cQED) using superconducting qubits remains a highly promising platform for realizing such a thermal machine, owing largely to the exceptional control that experimentalists have over the collective quantum degrees of freedom [12–14]. cQED has enjoyed a striking period of advancement, with numerous studies demonstrating strong coupling of photons to various types of qubits [15–17], with a broad range of applications [18–20]. Furthermore, modern nanofabrication techniques allow the integration and characterization of superconducting qubits coupled to normal-metal dissipative elements [21], creating hybrid cQED systems capable of probing thermal transport in quantum systems. Such systems differentiate themselves from previous attempts on quantum heat engines via their unambiguous implementation of thermal reservoirs, which naturally define the bath temperature, and possess a multitude of techniques for both primary and secondary thermometry [22,23].

Superconducting quantum circuits involving dissipative elements have already platformed several pioneering experiments in quantum heat transport. A transmon qubit coupled to two superconducting resonators, terminated by normal-metal resistors, has been used to measure dc heat

---

*andrew.guthrie@aalto.fi
†christoforus.satrya@aalto.fi

064022-1

transport modulated by magnetic flux threading a super-conducting quantum interference (SQUID) loop. By using both identical and nonidentical resonator frequencies, this has led to the realization of a quantum heat valve [24] and a quantum heat rectifier [25]. Despite the remarkable control exhibited by such systems, gigahertz-frequency cyclic driving of transmon qubits has proven experimentally difficult due to the large power dissipated by on-chip magnetic flux bias lines. Additionally, the performance of transmon qubits in thermal systems is limited by the relatively weak anharmonicity due to the large ratio of Josephson energy to charging energy, E_J/E_C. Weak anharmonicity removes the ability to properly isolate a qubit transition, meaning that contributions from higher energy levels create undesired parasitic coupling [25]. Moreover, the relatively long coherence time of a transmon qubit, a key asset in quantum-information applications, can limit the performance of cyclic quantum engines due to the build-up of coherences in a process known as "quantum friction" [26,27]. The theoretical operation of qubits as thermal machines has been explored extensively, with promising proposals for implementing both refrigerators [6,7,28–31] and heat engines [3,32–36].

To address the aforementioned problems in realizing a cyclic quantum refrigerator, a Cooper-pair box (charge qubit), which is isolated from higher energy states and easily modulated by an electric field, could be used as a working substance. A charge qubit, in its simplest form, consists of a nanoscale superconducting island, grounded though a Josephson junction [37]. Due to the small island dimension, the qubit frequency can now be tuned via the offset charge, N_g, on the island—controllable via the voltage of a nearby gate. Charge qubits have seen extensive study, both individually [38–40] and embedded in microwave cavities [41–44]. The strong coupling of a single photon to a charge qubit has been demonstrated in a pioneering work of cQED [15]. Furthermore, modulated dc heat transport through a charge-sensitive superconducting single-electron transistor has been realized and explained with a simple theoretical model [45]. Charge qubits have experienced diminishing popularity in recent years, since their charge sensitivity [46] leads to high dephasing rates in quantum-information applications. Nonetheless, their charge-sensitive properties could be exploited to create an efficient working substance that could be operated with remarkably small input signals. We further note that a charge-sensitive qubit connecting two cavity resonators could be a fundamental component in the field of quantum-information processing. The setup could allow interactions between distant transmon qubits to be controlled using voltage gates rather than magnetic flux lines—significantly reducing the power required to realize two-qubit gates, compared to tunable flux qubits or SQUIDs [47].

In this work, we experimentally demonstrate a charge-sensitive qubit capacitively coupled to two $\lambda/4$ resonators of differing frequency. We utilize a charge qubit consisting of an 8-nm-thick and 12-μm-long superconducting island connected to ground through a single Josephson junction. The use of a single junction, rather than the more common two-junction SQUID approach, allows us to achieve higher E_c while reducing the sensitivity of the qubit frequency to stray magnetic fields. Furthermore, we implement the ability for gigahertz driving of the qubit via an on-chip voltage gate in close proximity. Through a custom gate-line filtering scheme, we can prevent microwave leakage from the resonators and decay of the qubit, while maintaining the ability to drive at gigahertz frequencies. Our results show that, despite the submicrometer island dimensions, we can realize strong coupling of the qubit with two high-Q resonators without creating any spurious hybridized modes of the system. We go on to discuss how the measured device could be modified to operate as a quantum refrigerator and perform numerical simulations using a Markovian master equation [48,49].

II. COOPER-PAIR BOX COUPLED TO TWO RESONATORS

We consider a charge qubit operating deep in the charge-sensitive regime ($E_c \sim 2E_J$), which couples with two resonators with different frequency. Here, the energy states correspond closely to the charge states, $|N\rangle$, on the island and the Hamiltonian of the bare qubit is given by [37]

$$H_Q = \sum_N \Big[4E_c(N - N_g)^2 |N\rangle\langle N| \\ - \frac{E_J}{2}(|N\rangle\langle N+1| + |N+1\rangle\langle N|) \Big], \quad (1)$$

where $N_g = C_{\text{gate}}V_{\text{gate}}/2e$ is the dimensionless offset charge controlled by the nearby gate voltage V_{gate}, with capacitance C_{gate}. At sufficiently low temperature and with restricted N_g around the degeneracy point ($N_g = 0.5$), we can consider only two charge states, $|0\rangle$ and $|1\rangle$, and approximate the charge-qubit Hamiltonian as a two-level system, described by

$$H_Q = -2E_c(1 - 2N_g)\sigma^z - \frac{E_J}{2}\sigma^x, \quad (2)$$

where σ^z, σ^x are the corresponding 2×2 Pauli matrices in the charge basis. The energy transition of the qubit will be

$$\hbar\omega_Q = \sqrt{16E_c^2(1 - 2N_g)^2 + E_J^2}. \quad (3)$$

The qubit interacts capacitively with both voltage antinodes of two quarter-wavelength resonators. The Hamiltonian of each resonator is $H_{R,i} = hf_i a_i^\dagger a_i$ for $i =$

$\{c,h\}$, with the qubit-resonator interaction terms given by [16]

$$H_{I,i} = g_{i,0}(a_i^\dagger + a_i)[1 - 2N_g - \cos(\theta)\sigma^z + \sin(\theta)\sigma^x], \tag{4}$$

where $\theta = \arctan(E_J/4E_C(1 - 2N_g))$ is the qubit mixing angle. The atom-cavity coupling at the degeneracy point is determined by the zero-point energy fluctuations of the cavity electric potential and given by [46]

$$g_{i,0} = e\frac{C_i}{C_\Sigma}\sqrt{\frac{hf_i}{l_i\tilde{c}}}, \tag{5}$$

where C_i, C_Σ are the coupler-island and island total capacitances, respectively, l_i is the resonator length, and $\tilde{c}$ is the capacitance per unit length. By adding a term accounting for the resonator-resonator coupling, $\propto \tilde{g}$, the full-system Hamiltonian is therefore

$$H = H_Q + \sum_{i=c,h}(H_{R,i} + H_{I,i}) + \tilde{g}(a_c^\dagger a_h + a_h^\dagger a_c). \tag{6}$$

Operating close to the degeneracy point, the full Hamiltonian can be reduced to a simplified two-cavity Jaynes-Cummings-type Hamiltonian. The effective coupling strength g_i, i.e., the coupling strength when operating away from the degeneracy point in resonance with the respective resonator, is reduced by a factor of $\sin(\theta)$ in this framework. By implementing a time-dependent $N_g(t)$ field, the qubit transition frequency $\omega_Q(t)$ can be cyclically modulated to interact back and forth between the two resonators, f_c and f_h.

III. EXPERIMENTAL SETUP AND DEVICE

The measured device consists of a charge qubit, formed by a superconducting island connected to ground through a tunnel junction, capacitively coupled to two quarter-wavelength, coplanar-waveguide (CPW) resonators. A render of the device layout, along with the equivalent circuit, is shown in Figs. 1(a) and 1(b). In Fig. 1(b), it is depicted without the feedline. We fabricate the device on a 670-μm-thick and highly resistive silicon wafer. Ground planes, feedlines, couplers, and resonators are formed by reactive ion etching of a 200-nm niobium (Nb) film. The qubit is then formed using a Dolan-bridge technique to deposit two layers of aluminum (Al), with an *in situ* oxidation to form the tunnel junction. The Nb surface is milled *in situ* to ensure a clean contact between the Al and Nb film. Further detail on the fabrication procedure can be found in Appendix A.

The inset of Fig. 1(a) presents a scanning electron micrograph of the qubit, showing the 12-μm superconducting island, two Nb couplers, and the gate line. The

Josephson energy, $E_J = 3.5$ GHz, is controlled via the parameters of the oxidation and can be estimated by measuring the normal-state resistance ($R_N = 42$ kΩ) of replica junctions fabricated alongside the main structures. By using fork-shaped coupling structures on either side of the small superconducting island, we maximize the coupling strength by increasing the ratio C_i/C_Σ, as shown in Eq. (5). Using COMSOL simulations, we estimate the capacitances to be $C_c = C_h = 460$ aF and $C_{gate} = 5$ aF and the measured $C_\Sigma = 2.7$ fF, allowing a remarkable $C_i/C_\Sigma = 17\%$ to be achieved for each, which is competitively large even when compared with single-resonator systems [42,46].

The two resonators are terminated to ground close to a common feedline, creating inductive coupling to allow excitation and readout. By coupling both resonators to a single feedline, we perform single-tone spectroscopy of the qubit in a wide frequency range, confirming the interaction of the qubit with each resonator. The resonators are read out through a notch-type measurement, by measuring the scattering parameter, S_{21} [51]. Both resonators are overcoupled to the feedline (i.e., the coupling quality factor Q_c is less than the internal quality factor Q_i) to allow straightforward measurements in the single-photon regime. All measurements are performed in a cryogen-free dilution refrigerator, with a base temperature of 20 mK. A detailed diagram and further description of the measurement setup can be found in Appendix B. Figure 1(c) shows the calibrated S_{21} data as measured through the common feedline. Calibration is performed by measuring the same sample close to the critical temperature of the Nb film and then correcting via plotting $|S_{21}(20\text{-mK})/S_{21}(4\text{-K})|$. In this way, impedance mismatches due to the circuit are removed and only the temperature-dependent resonator structures remain. We can identify two peaks at $f_c = 4.718$ GHz and $f_h = 8.001$ GHz, corresponding to the two $\lambda/4$ resonators. We note the absence of any parasitic or hybridized modes, which suggests that the resonator-resonator crosstalk is small.

IV. SPECTROSCOPY OF THE RESONATOR-QUBIT-RESONATOR SYSTEM

To confirm the interaction of the qubit with each resonator, we perform simultaneous one-tone spectroscopy of the resonator-qubit-resonator system. We use a vector network analyzer (VNA) to probe a frequency, f_{probe}, in the vicinity of the two resonator frequencies, while varying the dc gate voltage. The number of photons in the cavity is estimated to be less than 1 in both cases. Figure 2 shows the one-tone spectra in the proximity of the two frequencies, as a function of the dimensionless offset charge, N_g. The Rabi splitting associated with the interaction of a two-level system with a cavity is shown clearly for the high-frequency resonator [Fig. 2(a)] and the low-frequency resonator [Fig. 2(b)]. Two periods are presented,
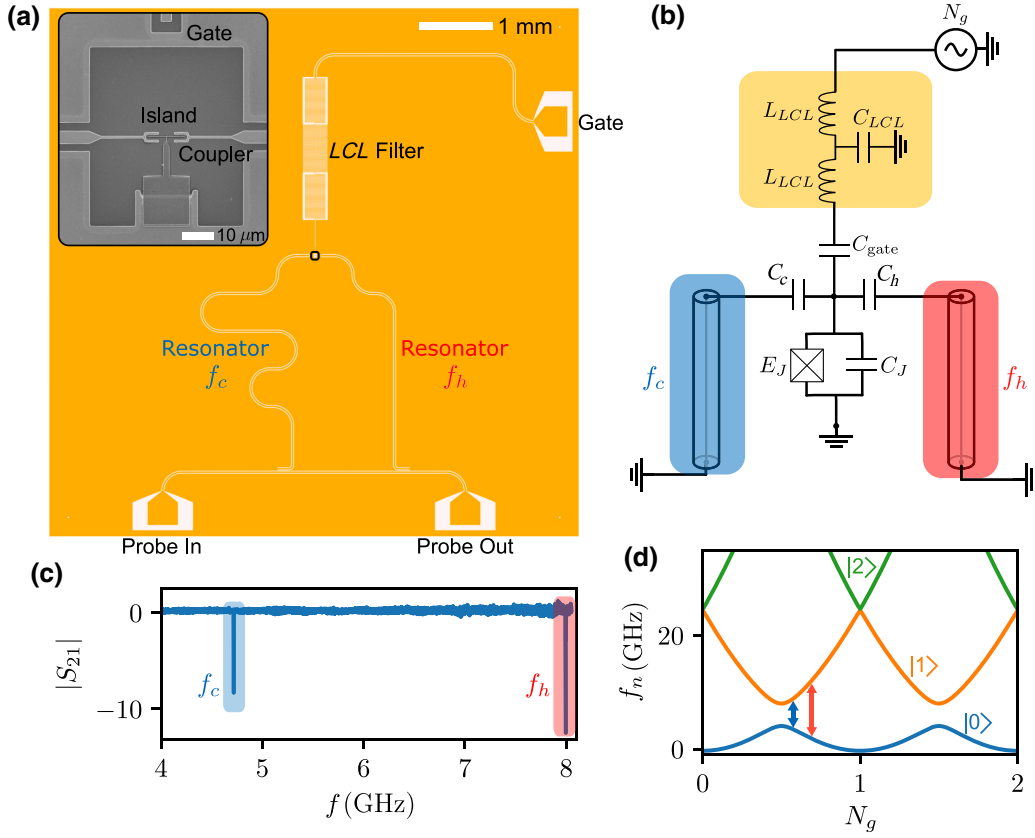
FIG. 1. (a) A design overview of the measured device. Two quarter-wavelength resonators of differing frequency are inductively coupled to a common feedline for readout. The voltage antinode of each resonator is capacitively coupled to a common superconducting island, connected to ground through a single Josephson junction (shown in the inset) and controllable by a nearby voltage gate. (b) The equivalent circuit for the measured sample with the feedline excluded. (c) Calibrated $|S_{21}(20\text{-mK})/S_{21}(4\text{-K})|$ transmission through the feedline, showing signals from two resonators and no spurious modes. (d) The calculated energy spectrum of the Cooper-pair box, showing the first three energy levels for $E_c/h = 6.8$ GHz and $E_J/h = 3.5$ GHz, clearly demonstrating high anharmonicity around the degeneracy point. The blue and red arrows indicate the level spacing corresponding to the low- and high-frequency resonators, respectively.

symmetrically around $N_g = 1$. The solid white lines are fits using the numerical solutions to Eq. (6), with $E_C/h = 6.8$ GHz and $E_J/h = 3.5$ GHz, showing excellent agreement with the theoretical model.

In our Cooper-pair box, the spatial profile of the superconducting gap energy is controlled by a thickness difference between the Al island and Al lead to suppress the quasiparticle-tunneling rate across the junction [52]. As a result, we observe one-Cooper-pair periodicity of the Rabi splitting in the one-tone spectroscopy. Nevertheless, the poisoning is still expected to be present close to the degeneracy point $N_g = 0.5$ [53]. This poisoning can be observed by the presence of some leftover signal at the cavity frequency in both cases, providing some remaining off-resonance qubit signal [54,55]. We observe this averaging effect because the average parity-switching rate is much shorter than the measurement time. By comparison of the relative amplitudes of the bare resonance signal with that of the remaining signal at the

degeneracy, we can estimate the parity preference for the odd and even states. We find an even-state preference of 66% and 61% in the case of the high-frequency and low-frequency resonators, respectively. This could be further mitigated through improved infrared shielding and further quasiparticle engineering [56]. In fact, quasiparticle tunneling is the dominant source of longitudinal relaxation, further discussed in Sec. V.

The relative coupling strengths are measured to be $g_{c,0}/2\pi = 140$ MHz, $g_{h,0}/2\pi = 250$ MHz, and $\tilde{g} \sim 0$. The negligible crosstalk is apparent in Fig. 1(c) from the lack of hybridized modes in the S_{21} spectrum and is expected due to the vanishing spectral overlap of the Lorentzian functions of the two resonators. We note the relatively weak signals for the dressed states as they move far from the cavity frequency, indicative of the higher dissipation associated with charge-sensitive devices when compared with transmon-type qubits. Although the raw couplings, $g_{c,0}$ and $g_{h,0}$, are large, due to the charge
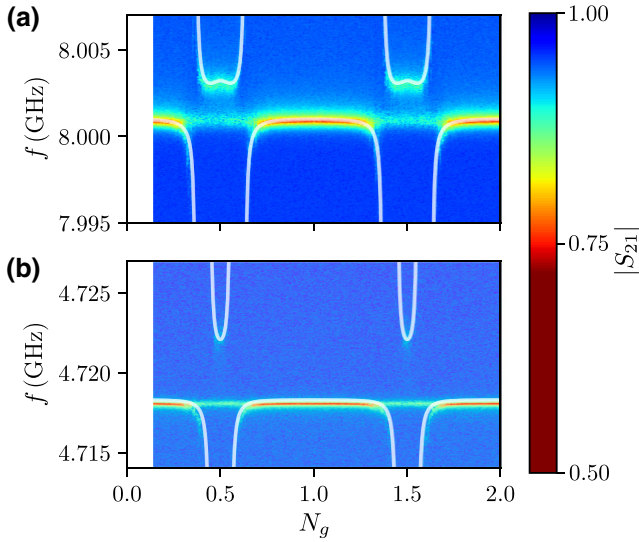
FIG. 2. Spectroscopy of the resonator-qubit-resonator system, showing interaction of the charge qubit with both resonators. Avoided crossings are shown with (a) a high-frequency resonator (f_h) and (b) a low-frequency resonator (f_c). The results from both resonators are collected simultaneously to remove charge bias offsets. The solid white lines are simulated eigenenergies of the system, calculated using the SCQUBITS [50] package to diagonalize the full Hamiltonian in Eq. (6). The model is calculated for $E_C/h = 6.8$ GHz, $E_J/h = 3.5$ GHz, $g_{c,0}/2\pi = 140$ MHz, $g_{h,0}/2\pi = 250$ MHz, and $\tilde{g} = 0$.

sensitivity the effective couplings are reduced by a factor of $\sin\theta$ and decrease as we move away from the degeneracy point. We extract the effective coupling strengths by measuring the dispersive shift, χ_i, of the resonance at the degeneracy point and calculate by $g_i = \sqrt{\chi_i \Delta_i}$, where $\Delta_i = (f_i - E_J/h)$ is the detuning at degeneracy. The effective coupling strengths are $g_h/2\pi = 125$ MHz and $g_c/2\pi = 76$ MHz, corresponding to 1.6% and 2% of the resonance frequency, respectively. Furthermore, the extracted E_J and E_C can be confirmed experimentally using a two-tone spectroscopy technique, to probe the exact qubit transition in the vicinity of the degeneracy point, discussed in detail in Sec. V.

Importantly, due to the large E_c and C_{gate} in the measured device, we can achieve qubit control in a large frequency range using remarkably small signals. Based upon the measured system parameters, the qubit could be driven sinusoidally between the two resonators using a signal amplitude $V_{\text{rms}} = 1.2$ mV, corresponding to just 10 nW power at 50 Ω. This presents a 4-orders-of-magnitude improvement over a comparable driving scheme using an on-chip magnetic flux bias line. Furthermore, the presented data also demonstrate a *charge-sensitive* qubit as a coupling element between two superconducting resonators.

V. DECOHERENCE OF THE CHARGE QUBIT

In order to quantify the qubit decoherence and to map the two lowest energy levels of the Cooper-pair box, two-tone spectroscopy is performed. The transmission, S_{21}, of a weak microwave signal (probe signal) is continuously measured by a VNA located at room temperature. The system is probed at the bare-resonance frequency of the high-frequency resonator ($f_{\text{probe}} = 8.001$ GHz), which is sensitive to the qubit population. The second signal (pump signal) is generated by a built-in second generator of the same VNA and combined using a signal splitter. When the pump frequency is in resonance with the qubit frequency, the qubit is excited and the measured probe S_{21} drops. By repeating this procedure at different N_g, the qubit energy spectrum can be traced. Figure 3(a) is the spectrum obtained and fitted well by the f_{01} transition, calculated from the Hamiltonian in Eq. (6) using SCQUBITS, obtaining $E_c/h = 6.8$ GHz and $E_J/h = 3.5$ GHz, in agreement with the results obtained in Sec. IV. The inset in Fig. 3(a) shows a slice at $N_g = 0.5$ (blue line) and is fitted by a Lorentzian function (orange line) with a line width δf.

The population of the excited state under continuous pumping, p_1, can be found from the steady-state solution to the Bloch equations and is given by [57]

$$p_1 = \frac{1}{2} \frac{4 n_p g_h^2 / (\Gamma_{1,\downarrow} \Gamma_{2,\downarrow})}{1 + ((f_Q - f_{\text{pump}})/\Gamma_{2,\downarrow})^2 + 4 n_p g_h^2 / \Gamma_{1,\downarrow} \Gamma_{2,\downarrow}}, \quad (7)$$

where g_h is the coupling strength to the readout resonator, in this case the high-frequency resonator. By fitting with a Lorentzian, we find that the spectral line width is related to the longitudinal-relaxation rate, $\Gamma_{1,\downarrow}$, and the phase-decoherence rate, $\Gamma_{2,\downarrow}$, of the qubit by

$$2\pi \delta f = \Gamma_{2,\downarrow} \sqrt{1 + \frac{4 n_p g_h^2}{\Gamma_{1,\downarrow} \Gamma_{2,\downarrow}}}, \quad (8)$$

where n_p is the pump photon number.

Figure 3(b) presents the dependence of the spectral line width squared for varying pump power P_{pump}, showing the expected power dependence as $n_p \propto P_{\text{pump}}$. The dashed orange line shows a fit to the data using Eq. (8), allowing us to extract the spectral line width as $P_{\text{pump}} \to 0$ by extrapolation. Here, due to the low power of the pump signal, $n_p \to 0$, the line width δf is dominated by qubit dissipation [57]; thus $2\pi \delta f \sim \Gamma_{2,\downarrow}$, which is the qubit-decoherence rate. The dissipation measured by this approach can be decomposed to the two relaxation processes, longitudinal relaxation, $\Gamma_{1,\downarrow}$, and pure dephasing, Γ_φ, related through the expression

$$\Gamma_{2,\downarrow} = \frac{\Gamma_{1,\downarrow}}{2} + \Gamma_\varphi. \quad (9)$$

(a)

(b)

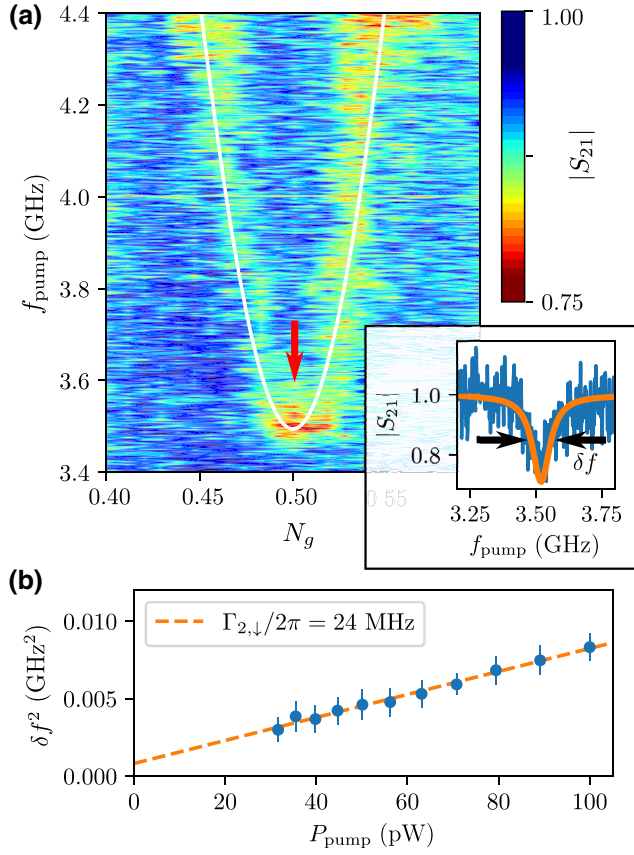
FIG. 3. (a) Two-tone spectroscopy of the charge qubit in the vicinity of the degeneracy point ($N_g = 0.5$), with fixed probe tone $f_{probe} = 8.001$ GHz and sweeping pump tone f_{pump} from 3.4 to 4.4 GHz. The solid white line indicates the transition energy of the two-level system qubit solved from the Hamiltonian in Eq. (6) using SCQUBITS, for $E_c/h = 6.8$ GHz and $E_J/h = 3.5$ GHz. The inset shows a frequency slice of two-dimensional data, as indicated by the red arrow, and is fitted using a Lorentzian function. (b) The squared spectral line width of the Lorentzian as a function of the pump power, P_{pump}, averaged by repeated sampling of the curves. The dashed orange line presents a fit using Eq. (8). By extrapolation ($P_{pump} \rightarrow 0$, $n_p \rightarrow 0$), we estimate the dephasing time to be $\Gamma_{2,\downarrow}/2\pi = 24$ MHz.

Although our measurement technique does not allow us to extract the relative size of each contribution, previous experiments suggest that longitudinal relaxation is dominant close to the degeneracy point, where quasiparticle tunneling is the major contributor [58].

VI. VOLTAGE DRIVING AND SUPPRESSION OF MICROWAVE LEAKAGE

In order to drive the qubit energy cyclically, sinusoidal or arbitrary voltage driving should be applied through the gate line to modulate the qubit energy level between the low-frequency (f_c) and high-frequency (f_h) resonator, without introducing noise or microwave leakage through the driving line. Quarter-wave ($\lambda/4$) resonators, which have
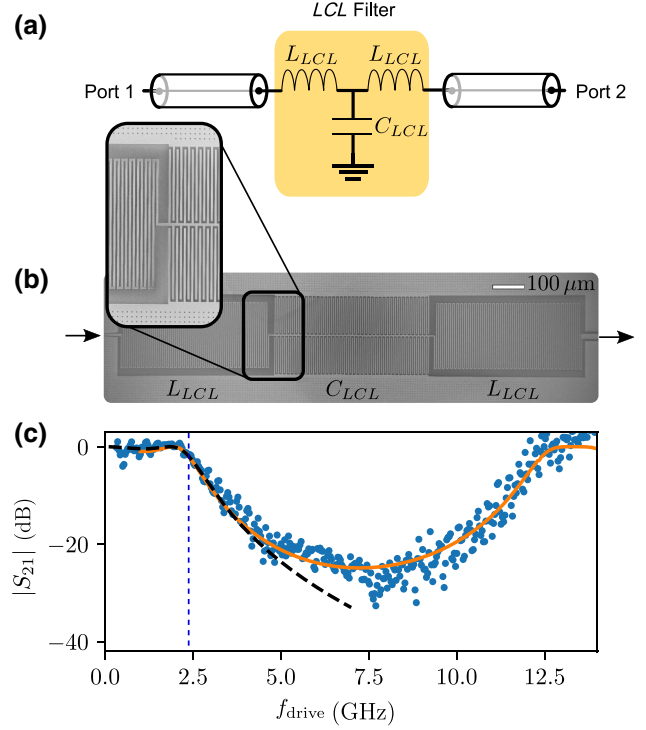
(a)

(b)

(c)

FIG. 4. (a) The schematic lumped circuit of the *LCL* filter, consisting of two series inductors grounded in the middle by a capacitor. (b) A scanning-electron-microscope (SEM) image of the fabricated *LCL* filter comprised of two Nb-film meandering-line inductors and an interdigitated capacitor. (c) Transmission spectra, S_{21}, between ports 1 and 2 for driving frequencies f_{drive} 0.1–14 GHz. Blue dots are measured data at 20 mK, while the solid orange line and black dashed line are the SONNET simulation and analytical model, respectively. The *LCL* cutoff frequency, $f_{cutoff} = 2.3$ GHz, is shown by the blue dashed line.

a voltage maximum at the open side, interact capacitively with the gate line, introducing some microwave leakage to the line. Filtering the operating range of the qubit (4–8 GHz) while allowing an ac signal up to few gigahertz is pivotal. We utilize a superconducting *LCL* circuit acting as a low-pass filter [59], enabling us to prevent microwave leakage with around 20 dB attenuation and to drive the qubit up to a cutoff frequency of few gigahertz. Figure 4(a) shows the schematic circuit of an *LCL* filter consisting of two series inductors shunted at the center by a capacitor. In the fabricated device, as shown in Fig. 4(b), the filter is realized by a meandering-line inductor (L_{LCL}) and an interdigitated capacitor (C_{LCL}), both with a central width and line spacing of 4 μm.

To understand the transmission properties, the filter is separately characterized at 20 mK, as shown in Fig. 4(c), by measuring S_{21} of a sinusoidal signal with frequency f_{drive} between ports 1 and 2. The blue dots in Fig. 4(c) show the calibrated S_{21} signal and exhibit close-to-100% transmission up to approximately 2.3 GHz and > 20 dB

attenuation within the range of 4–10 GHz. Above 10 GHz, the attenuation starts to decrease and reaches 0 dB at approximately 13 GHz. A lumped-circuit model of transmission derived from the *ABCD* matrix (dashed black line), discussed in detail in Appendix C, predicts the behavior of the filter up to approximately 4 GHz and deviates above it due to the parasitic capacitance of the meandering inductors, which is not taken into account in the model. From the fitting, the cutoff frequency $f_{\text{cutoff}} = \sqrt{2/L_{LCL}C_{LCL}}$ is obtained to be 2.3 GHz with $L_{LCL} = 5.9$ nH and $C_{LCL} = 1.7$ pF. A finite-element simulation using SONNET (orange line) captures fully the transmission of the filter, with excellent agreement. The characterized filter is capable of blocking microwave leakage within the frequency range of the two resonators, while still allowing cyclic driving of the qubit up to 2.3 GHz.

VII. PROPOSED OPERATION OF THE QUANTUM OTTO REFRIGERATOR

The measured device could be modified to operate as a quantum Otto refrigerator by terminating the two resonators by normal-metal resistors [6]. The resistor-terminated resonators act as a thermal bath [24,25]. Furthermore, by connecting superconducting probes to the resistors through an insulating barrier, the temperature of the two baths could be controlled and monitored through voltage and current bias, respectively [22]. Due to the dissipation created by the normal-metal probes, the quality factor of the resonators would be very low ($Q \sim 10$) [21] and qubit spectroscopic characterization could no longer be performed.

The Otto refrigerator cycle is the most practically achievable implementation of a quantum refrigerator. The Otto cycle consists of sequential interactions between a two-level system and a cold (f_c) and hot (f_h) reservoir. It has four branches: an adiabatic stroke of the qubit frequency from f_c to f_h, thermalization with the hot bath at frequency f_h, an adiabatic stroke back from f_h to f_c, and finally thermalization with the cold bath at frequency f_c. Cooling is achieved under the condition $f_h/f_c > T_h/T_c$, where T_h and T_c are the temperatures of the normal-metal elements shunting the hot and cold resonators to ground, respectively.

To implement the quantum Otto cycle in our system, we should consider Eq. (2); however, allowing time dependence in the offset charge $N_g(t)$. We consider driving the system with a truncated trapezoidal shape,

$$q(t) = \frac{1}{2}\left[1 + \frac{\tanh(a\cos(2\pi f_{\text{drive}}t))}{\tanh(a)}\right], \quad (10)$$

where a is a constant, a form previously demonstrated to yield a large cooling power [6]. The offset charge is applied

by gate voltage and driven in the form

$$N_g(t) = N_{g,c} + (N_{g,h} - N_{g,c})q(t), \quad (11)$$

where $N_{g,c}$ and $N_{g,h}$ are the offset charges at which the qubit interacts with the cold and hot reservoir, respectively, obtained from rearranging Eq. (3).

For a qubit coupled to a resonator, its emission rates are altered according to the Purcell effect, and can be calculated using Fermi's golden rule [46]. Following Ref. [6,60], we consider the dissipators to take the form of Johnson-Nyquist noise generated by a normal-metal resistor and spectrally filtered by the Lorentzian function of the resonators. The transition rates are therefore described by

$$\Gamma_{i,\downarrow}(t) = \frac{g_i}{4\pi} \frac{1}{1 + Q_i^2(\omega_i/\omega_Q - \omega_Q/\omega_i)^2} \frac{\omega_Q}{1 - e^{-\hbar\omega_Q/k_BT_i}}, \quad (12)$$

where $\omega_i = 2\pi f_i$ is the resonator frequency, Q_i is the associated quality factor, $\omega_Q(t)$ is the instantaneous qubit frequency, and T_i is the temperature of each normal-metal resistor terminating the resonator. The rates coming from the two heat baths obey the detailed balance condition as follows:

$$\Gamma_{i,\uparrow}(t) = \Gamma_{i,\downarrow}(t)\exp(-\hbar\omega_Q/k_BT_i). \quad (13)$$

In this way, the transition rates from each bath are maximized when the qubit is in resonance with the corresponding resonator frequency. Due to the finite quality factor of the resonators, this protocol can only approximate the Otto cycle, since the qubit is never fully decoupled from either bath. Furthermore, the cooling power at the highest drive frequencies is limited by these transition rates, since the cycle becomes too short for the qubit to reach equilibrium with the resonators.

In limit at which the bath-resonator coupling exceeds the resonator-qubit coupling (local limit) and, in the limit of slow driving, the evolution of the qubit density matrix can be described by a Lindblad master equation as [48]

$$\dot{\rho}(t) = \frac{-i}{\hbar}\left[H_Q, \rho(t)\right] + \Gamma_\uparrow(t)\left[\sigma_+\rho(t)\sigma_- - \frac{1}{2}\{\sigma_-\sigma_+, \rho(t)\}\right]$$
$$+ \Gamma_\downarrow(t)\left[\sigma_-\rho(t)\sigma_+ - \frac{1}{2}\{\sigma_+\sigma_-, \rho(t)\}\right], \quad (14)$$

where $\Gamma_{\uparrow/\downarrow}(t) = \Gamma_{c,\uparrow/\downarrow}(t) + \Gamma_{h,\uparrow/\downarrow}(t)$ are the qubit transition rates, $\sigma_\pm$ are the instantaneous jump operators of the system, and $\{a, b\}$ defines the anticommutator operation.

The equivalent heat-flow diagram, including two heat baths and the corresponding rates, is shown in Fig. 5. We simplify Eq. (14) by transforming to the rotating frame using $\bar{\rho} = V(t)^\dagger\rho V(t)$ [61], where V is the unitary matrix
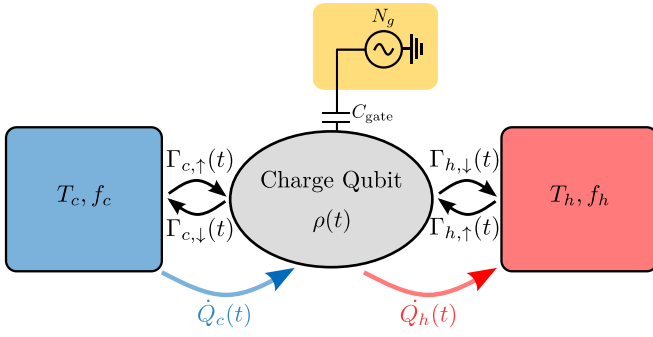
FIG. 5. The equivalent heat-flow diagram used for the numerical simulations of the quantum Otto refrigerator. We consider the case of two heat baths corresponding to the two resistor-terminated resonators.

diagonalizing $H_Q(t)$. Then, parametrizing in terms of the Bloch-equation elements $x(t)$, $y(t)$, and $z(t)$, the evolution results in the compact expressions

$$\dot{x}(t) = -\frac{\Gamma_\downarrow(t) + \Gamma_\uparrow(t)}{2}x(t) - \omega_Q(t)y(t) - \frac{8E_cE_J\dot{N}_g(t)}{\hbar^2\omega_Q^2}z(t),$$

(15)

$$\dot{y}(t) = \omega_Q(t)x(t) - \frac{\Gamma_\downarrow(t) + \Gamma_\uparrow(t)}{2}y(t),$$

(16)

$$\dot{z}(t) = \frac{8E_cE_J\dot{N}_g(t)}{\hbar^2\omega_Q(t)^2}x(t) - [\Gamma_\downarrow(t) + \Gamma_\uparrow(t)]z(t)$$
$$- [\Gamma_\downarrow(t) - \Gamma_\uparrow(t)].$$

(17)

Based on this, we further note that the condition for adiabatic evolution in our system is [62]

$$\frac{\langle 0|\dot{H}|1\rangle}{h^2\omega_Q^2} \ll 1,$$

(18)

where fulfillment means that the system remains in an instantaneous eigenstate throughout the evolution. Furthermore, we can write the exact heat currents from each bath in terms of the elements of the Bloch vector as

$$\dot{Q}_i(t) = \frac{-\hbar\omega_Q(t)}{2}\left([\Gamma_{i,\downarrow(t)} + \Gamma_{i,\uparrow(t)}]z(t) + [\Gamma_{i,\downarrow(t)} - \Gamma_{i,\uparrow(t)}]\right).$$

(19)

Figure 6 shows the average power extracted from the hot and cold baths, $\langle\dot{Q}_i\rangle = 1/\tau\int_0^\tau \dot{Q}_i(t)dt$, as the red and blue solid lines for the measured system parameters, averaged over one cycle once the system has reached the steady state. Furthermore, it can be seen that the rate of entropy production is consistent according to the second law: $\dot{S} - \sum_i \dot{Q}_i/k_BT_i \geq 0$.

Interestingly, the driving rate in our system could be high enough to observe quantum behavior in the refrigerator cooling power, whereby off-diagonal terms in the
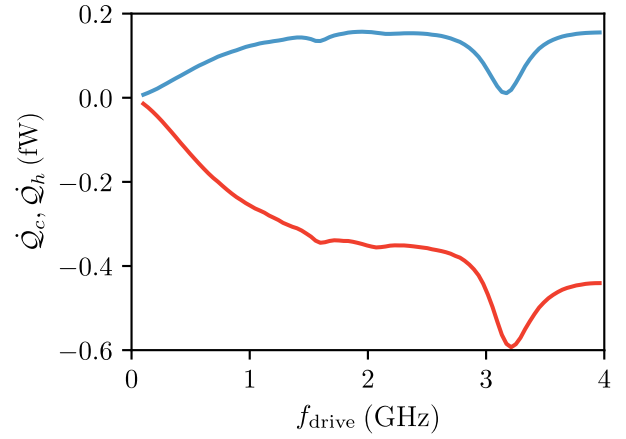

FIG. 6. Numerical simulations of the cooling power in a Cooper-pair box acting as a quantum Otto refrigerator for realistic values of the resonators quality factor $Q_c = Q_h = 2$ [21, 24,25], $T_c = T_h = 300$ mK, and with $a = 2$. The rising (blue) curve shows the heat extracted (positive) from the cold bath and the falling (red) curve shows the heat extracted (negative) to the hot bath. At the highest drive frequencies, we could achieve approximately 150 aW of cooling power, detectable using standard normal-metal–insulator–superconductor (*N*-*I*-*S*) thermometry techniques.

density matrix, ρ, could begin to affect the refrigerator performance. In the simulations, the quantum effects are clearly visible by sharp oscillations in the cooling power at high values of f_{drive}, as has been seen in previous theoretical studies involving qubit Otto refrigerators [6]. Dips are created when the frequency of the free-qubit rotation about the Bloch sphere matches the driving frequency. In the future, to suppress this behavior, a counterdiabatic driving protocol could be implemented, which generally consists of an additional field to "guide" the qubit along an adiabatic trajectory [60]. We note, however, that for very fast driving, the Lindblad operators may no longer be jump operators between the instantaneous eigenstates of the Hamiltonian. The modeling could be further improved by utilizing more advanced Floquet master equations, as has been done in Ref. [36], for example.

In addition to the direct heat flows discussed here, tunneling quasiparticles in the system will also affect the refrigerator performance. We see experimental evidence of this effect from the noninteracting portion of the signal seen in Figs. 2(a) and 2(b). Since each tunneling quasiparticle shifts the qubit transition off-resonance, we can understand this effect as a reduction in the effective coupling strength to each resonator, i.e., $\bar{g}_c = 0.61g_c$ and $\bar{g}_h = 0.66g_h$. Incorporating such an effect into the numerics reduces the peak cooling power from 150 aW to 60 aW, which is still detectable using standard normal-metal–insulator–superconductor (*N*-*I*-*S*) thermometry techniques. However, this highlights the importance of further quasiparticle mitigation strategies.

VIII. CONCLUSIONS

In summary, a charge-sensitive qubit is coupled to two superconducting coplanar waveguides, with the ability to drive the qubit over a large frequency range using remarkably small excitations. Additionally, the measured effective coupling strength of the qubit to each resonator remains exceptionally high, competitive with the highest previously measured in charge-sensitive devices. Furthermore, we demonstrate that despite the close proximity of the various coupling elements, our system can be simply described within the framework of a two-level qubit interacting with two resonators. Utilizing the measured device parameters, we propose and simulate the operation of our device acting as a quantum Otto refrigerator and show cooling powers of the order of approximately 60 aW, which are detectable using normal-metal–insulator–superconductor (NIS). Additionally, the measured system could be used to realize a highly effective heat rectifier, owing to the large anharmonicity of the charge qubit, allowing the isolation of a single-qubit transition. Our work lays the technical foundation for the realization of cyclic quantum heat engines within the cQED framework and may open the door toward a multitude of future studies in the field of quantum thermodynamics.

All data used in this paper are available upon request to the authors, including descriptions of the data sets and scripts to generate the figures.

APPENDIX A: FABRICATION DETAILS

The fabrication of the device is done in a multistage process on a 675-μm-thick and highly resistive silicon substrate. The fabrication consists of two main steps: patterning microwave structures on a Nb film and Josephson-junction elements on an Al film. A 40-nm-thick Al_2O_3 layer is deposited onto a silicon substrate using atomic
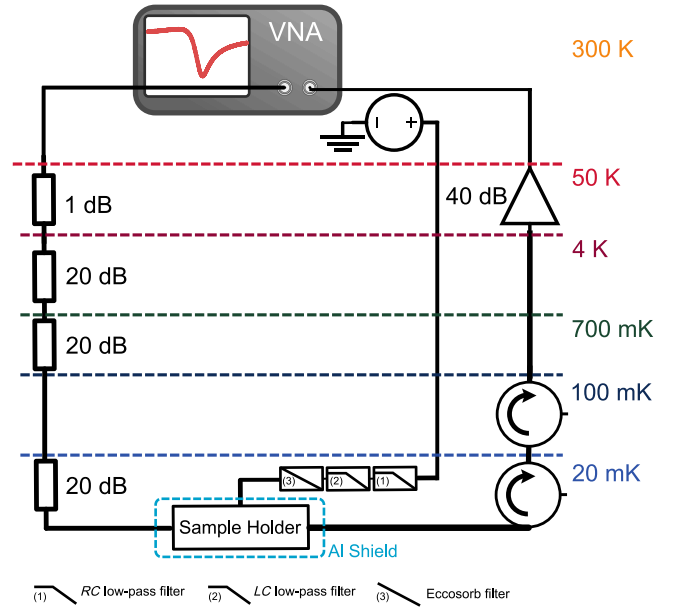

FIG. 7. A schematic of the experimental setup used for one- and two-tone spectroscopy measurements. The rf measurements are performed using a vector network analyzer (VNA) to measure S_{21} through the sample, though a series of cryogenic attenuators, and amplified through cryogenic and room-temperature amplifiers. The offset charge N_g is controlled by a voltage source, connected through resistive thermocoax wiring to the mixing chamber. The voltage signal is further filtered through RC (cutoff 20 kHz) and LC (cutoff 80 MHz) and infrared (Eccosorb) filters.

layer deposition, followed by a deposition of a 200-nm-thick Nb film using dc magnetron sputtering. Positive electron-beam resist, AR-P6200.13, is spin coated with a speed of 5500 rpm (revolutions per minute) for 60 s and is postbaked for 9 min at 150°C, after which it is patterned by electron-beam lithography (EBL) and etched by reactive ion etching. A shadow mask defined by EBL on a 1-μm-thick poly(methyl-metacrylate)–copolymer resist bilayer is used to fabricate the Al island and Josephson junction using a two-angle deposition technique at 0° and 32° sequentially. Before the deposition, the Nb surface is cleaned *in situ* by Ar ion-plasma milling for 45 s, followed by the first 8-nm-thick Al island deposition. The island is then oxidized at a pressure of 2.5 mbar for 2.5 min to form a tunnel barrier before depositing the second 100-nm Al film. Finally, after liftoff in acetone and isopropyl alcohol, the substrate is cut by an automatic dicing-saw machine to the size 7 × 7 mm and wire bonded to a rf holder for the low-temperature characterization.

APPENDIX B: EXPERIMENTAL DETAILS

Measurements are performed in a cryogen-free dilution refrigerator with a base temperature of 20 mK. Using a VNA, a probe microwave tone is supplied to the feedline through a 80 dB of attenuation distributed at the various

temperature stages of the cryostat. The probe signal is then passed through two cryogenic circulators, before being amplified first by a 40 dB cryogenic amplifier and then by a 40 dB room-temperature amplifier, as shown in Fig. 7. The offset charge, N_g, is supplied by a nearby voltage gate, with the dc component passed though a low-temperature RC filter, LC filter, and Eccosorb filter, and connected to an isolated voltage source at room temperature. The device is mounted in a tight Cooper holder and covered by an Al shield to protect it from stray magnetic fields and incident radiation.

APPENDIX C: *LCL*-FILTER TRANSMISSION

The 2×2 transmission matrix, or *ABCD* matrix, of a network is constructed by multiplying the *ABCD* matrices of each individual two-port element sequentially [63]. In the case of the *LCL* network, the *ABCD* matrix is given by the multiplication of *ABCD* matrices of the inductor (Z_L) in series, the capacitor (Z_C) in parallel, and the inductor (Z_L) in series, as schematically shown in Fig. 4(a) and formulated as follows:

$$\begin{pmatrix} A & B \\ C & D \end{pmatrix} = \begin{pmatrix} 1 & Z_L(f) \\ 0 & 1 \end{pmatrix} \begin{pmatrix} 1 & 0 \\ 1/Z_C(f) & 1 \end{pmatrix} \begin{pmatrix} 1 & Z_L(f) \\ 0 & 1 \end{pmatrix}. \tag{C1}$$

The voltage ratio between ports 2 and 1 (S_{21}), can then be calculated as

$$S_{21}(f) = \frac{2}{A + B/Z_0 + CZ_0 + D} \tag{C2}$$

$$S_{21}(f) = \frac{2Z_0 Z_C}{2Z_0(Z_L + Z_C) + (2Z_L Z_C + Z_L^2) + Z_0^2} \tag{C3}$$

where $Z_L = j2\pi f L_{LCL}$, $Z_C = j/(2\pi f C_{LCL})$, and $Z_0 = 50\ \Omega$; L_{LCL} and C_{LCL} are the inductance and capacitance values of the *LCL* filter.

---

[1] R. Kosloff and A. Levy, Quantum heat engines and refrigerators: Continuous devices, Annu. Rev. Phys. Chem. **65**, 365 (2014).

[2] R. Alicki, The quantum open system as a model of the heat engine, J. Phys. A: Math. Gen. **12**, L103 (1979).

[3] H. T. Quan, Yu-xi. Liu, C. P. Sun, and F. Nori, Quantum thermodynamic cycles and quantum heat engines, Phys. Rev. E **76**, 031105 (2007).

[4] F. Binder, L. A. Correa, C. Gogolin, J. Anders, and G. Adesso, *Thermodynamics in the Quantum Regime* (Springer-Verlag, Cham, Switzerland, 2019).

[5] R. Kosloff, Quantum thermodynamics: A dynamical viewpoint, Entropy **15**, 2100 (2013).

[6] B. Karimi and J. P. Pekola, Otto refrigerator based on a superconducting qubit: Classical and quantum performance, Phys. Rev. B **94**, 184503 (2016).

[7] A. O. Niskanen, Y. Nakamura, and J. P. Pekola, Information entropic superconducting microcooler, Phys. Rev. B **76**, 174523 (2007).

[8] J. Roßnagel, S. T. Dawkins, K. N. Tolazzi, O. Abah, E. Lutz, F. Schmidt-Kaler, and K. Singer, A single-atom heat engine, Science **352**, 325 (2016).

[9] M. Josefsson, A. Svilans, A. M. Burke, E. A. Hoffmann, S. Fahlvik, C. Thelander, M. Leijnse, and H. Linke, A quantum-dot heat engine operating close to the thermodynamic efficiency limits, Nat. Nanotechnol. **13**, 920 (2018).

[10] J. P. S. Peterson, T. B. Batalhão, M. Herrera, A. M. Souza, R. S. Sarthour, I. S. Oliveira, and R. M. Serra, Experimental Characterization of a Spin Quantum Heat Engine, Phys. Rev. Lett. **123**, 240601 (2019).

[11] K. Ono, S. N. Shevchenko, T. Mori, S. Moriyama, and F. Nori, Analog of a Quantum Heat Engine Using a Single-Spin Qubit, Phys. Rev. Lett. **125**, 166802 (2020).

[12] J. Q. You and F. Nori, Superconducting circuits and quantum information, Phys. Today **58**, 42 (2005).

[13] X. Gu, A. F. Kockum, A. Miranowicz, Y.-x. Liu, and F. Nori, Microwave photonics with superconducting quantum circuits, Phys. Rep. **718-719**, 1 (2017).

[14] M. Kjaergaard, M. E. Schwartz, J. Braumüller, P. Krantz, J. I.-J. Wang, S. Gustavsson, and W. D. Oliver, Superconducting qubits: Current state of play, Annu. Rev. Condens. Matter Phys. **11**, 369 (2020).

[15] A. Wallraff, D. I. Schuster, A. Blais, L. Frunzio, R.-S. Huang, J. Majer, S. Kumar, S. M. Girvin, and R. J. Schoelkopf, Strong coupling of a single photon to a superconducting qubit using circuit quantum electrodynamics, Nature **431**, 162 (2004).

[16] A. Blais, R.-S. Huang, A. Wallraff, S. M. Girvin, and R. J. Schoelkopf, Cavity quantum electrodynamics for superconducting electrical circuits: An architecture for quantum computation, Phys. Rev. A **69**, 062320 (2004).

[17] D. I. Schuster, A. A. Houck, J. A. Schreier, A. Wallraff, J. M. Gambetta, A. Blais, L. Frunzio, J. Majer, B. Johnson, M. H. Devoret, S. M. Girvin, and R. J. Schoelkopf, Resolving photon number states in a superconducting circuit, Nature **445**, 515 (2007).

[18] J. Clarke and F. K. Wilhelm, Superconducting quantum bits, Nature **453**, 1031 (2008).

[19] A. Montanaro, Quantum algorithms: An overview, npj Quantum Inf. **2**, 15023 (2016).

[20] G. Wendin, Quantum information processing with superconducting circuits: A review, Rep. Prog. Phys. **80**, 106001 (2017).

[21] Y.-C. Chang, B. Karimi, J. Senior, A. Ronzani, J. T. Peltonen, H.-S. Goan, C.-D. Chen, and J. P. Pekola, Utilization of the superconducting transition for characterizing low-quality-factor superconducting resonators, Appl. Phys. Lett. **115**, 022601 (2019).

[22] F. Giazotto, T. T. Heikkilä, A. Luukanen, A. M. Savin, and J. P. Pekola, Opportunities for mesoscopics in thermometry and refrigeration: Physics and applications, Rev. Mod. Phys. **78**, 217 (2006).

[23] J. P. Pekola and B. Karimi, Colloquium: Quantum heat transport in condensed matter systems, Rev. Mod. Phys. **93**, 041001 (2021).

[24] A. Ronzani, B. Karimi, J. Senior, Y.-C. Chang, J. T. Peltonen, C. Chen, and J. P. Pekola, Tunable photonic heat

transport in a quantum heat valve, Nat. Phys. **14,** 991 (2018).

[25] J. Senior, A. Gubaydullin, B. Karimi, J. T. Peltonen, J. Ankerhold, and J. P. Pekola, Heat rectification via a superconducting artificial atom, Commun. Phys. **3,** 40 (2020).

[26] P. A. Camati, J. F. G. Santos, and R. M. Serra, Coherence effects in the performance of the quantum Otto heat engine, Phys. Rev. A **99,** 062103 (2019).

[27] A. R. Insinga, The quantum friction and optimal finite-time performance of the quantum Otto cycle, Entropy **22,** 1060 (2020).

[28] M. Kloc, K. Meier, K. Hadjikyriakos, and G. Schaller, Superradiant Many-Qubit Absorption Refrigerator, Phys. Rev. Appl. **16,** 044061 (2021).

[29] O. Abah and E. Lutz, Optimal performance of a quantum Otto refrigerator, EPL (Europhysics Letters) **113,** 60002 (2016).

[30] K. Brandner and U. Seifert, Periodic thermodynamics of open quantum systems, Phys. Rev. E **93,** 062134 (2016).

[31] J. P. Pekola, B. Karimi, G. Thomas, and D. V. Averin, Supremacy of incoherent sudden cycles, Phys. Rev. B **100,** 085405 (2019).

[32] P. P. Hofer, J.-R. Souquet, and A. A. Clerk, Quantum heat engine based on photon-assisted Cooper pair tunneling, Phys. Rev. B **93,** 041418 (2016).

[33] M. Campisi and R. Fazio, The power of a critical heat engine, Nat. Commun. **7,** 11895 (2016).

[34] A. Solfanelli, M. Falsetti, and M. Campisi, Nonadiabatic single-qubit quantum Otto engine, Phys. Rev. B **101,** 054513 (2020).

[35] T. D. Kieu, The Second Law, Maxwell's Demon, and Work Derivable from Quantum Heat Engines, Phys. Rev. Lett. **93,** 140403 (2004).

[36] D. Gelbwaser-Klimovsky, R. Alicki, and G. Kurizki, Minimal universal quantum heat machine, Phys. Rev. E **87,** 012140 (2013).

[37] Y. V. Nazarov and Y. M. Blanter, *Quantum Transport: Introduction to Nanoscience* (Cambridge University Press, Cambridge, 2009).

[38] Y. Nakamura, Yu. A. Pashkin, and J. S. Tsai, Coherent control of macroscopic quantum states in a single-Cooper-pair box, Nature **398,** 786 (1999).

[39] Yu. A. Pashkin, O. Astafiev, T. Yamamoto, Y. Nakamura, and J. S. Tsai, Josephson charge qubits: A brief review, Quantum Inf. Process. **8,** 55 (2009).

[40] K. Bladh, T. Duty, D. Gunnarsson, and P. Delsing, The single Cooper-pair box as a charge qubit, New J. Phys. **7,** 180 (2005).

[41] M. Sillanpää, T. Lehtinen, A. Paila, Y. Makhlin, and P. Hakonen, Continuous-Time Monitoring of Landau-Zener Interference in a Cooper-Pair Box, Phys. Rev. Lett. **96,** 187002 (2006).

[42] O. Astafiev, K. Inomata, A. O. Niskanen, T. Yamamoto, Yu. A. Pashkin, Y. Nakamura, and J. S. Tsai, Single artificial-atom lasing, Nature **449,** 588 (2007).

[43] Z. Kim, V. Zaretskey, Y. Yoon, J. F. Schneiderman, M. D. Shaw, P. M. Echternach, F. C. Wellstood, and B. S. Palmer, Anomalous avoided level crossings in a Cooper-pair box spectrum, Phys. Rev. B **78,** 144506 (2008).

[44] Z. Kim, B. Suri, V. Zaretskey, S. Novikov, K. D. Osborn, A. Mizel, F. C. Wellstood, and B. S. Palmer, Decoupling a Cooper-Pair Box to Enhance the Lifetime to 0.2 ms, Phys. Rev. Lett. **106,** 120501 (2011).

[45] O. Maillet, D. Subero, J. T. Peltonen, D. S. Golubev, and J. P. Pekola, Electric field control of radiative heat transfer in a superconducting circuit, Nat. Commun. **11,** 4326 (2020).

[46] J. Koch, T. M. Yu, J. Gambetta, A. A. Houck, D. I. Schuster, J. Majer, A. Blais, M. H. Devoret, S. M. Girvin, and R. J. Schoelkopf, Charge-insensitive qubit design derived from the Cooper pair box, Phys. Rev. A **76,** 042319 (2007).

[47] R. Stassi, M. Cirio, and F. Nori, Scalable quantum computer with superconducting circuits in the ultrastrong coupling regime, npj Quantum Inf. **6,** 67 (2020).

[48] G. Lindblad, On the generators of quantum dynamical semigroups, Commun. Math. Phys. **48,** 119 (1976).

[49] F. Petruccione and H.-P. Breuer, *The Theory of Open Quantum Systems* (Oxford University Press, Oxford, United Kingdom, 2007).

[50] P. Groszkowski and J. Koch, Scqubits: A Python package for superconducting qubits, Quantum **5,** 583 (2021).

[51] S. Probst, F. B. Song, P. A. Bushev, A. V. Ustinov, and M. Weides, Efficient and robust analysis of complex scattering data under noise in microwave resonators, Rev. Sci. Instrum. **86,** 024706 (2015).

[52] T. Yamamoto, Y. Nakamura, Yu. A. Pashkin, O. Astafiev, and J. S. Tsai, Parity effect in superconducting aluminum single electron transistors with spatial gap profile controlled by film thickness, Appl. Phys. Lett. **88,** 212509 (2006).

[53] J. Aumentado, M. W. Keller, J. M. Martinis, and M. H. Devoret, Nonequilibrium Quasiparticles and 2*e* Periodicity in Single-Cooper-Pair Transistors, Phys. Rev. Lett. **92,** 066802 (2004).

[54] L. Sun, L. DiCarlo, M. D. Reed, G. Catelani, L. S. Bishop, D. I. Schuster, B. R. Johnson, G. A. Yang, L. Frunzio, L. Glazman, M. H. Devoret, and R. J. Schoelkopf, Measurements of Quasiparticle Tunneling Dynamics in a Band-Gap-Engineered Transmon Qubit, Phys. Rev. Lett. **108,** 230509 (2012).

[55] K. Serniak, S. Diamond, M. Hays, V. Fatemi, S. Shankar, L. Frunzio, R. Schoelkopf, and M. Devoret, Direct Dispersive Monitoring of Charge Parity in Offset-Charge-Sensitive Transmons, Phys. Rev. Appl. **12,** 014052 (2019).

[56] G. Catelani and J. P. Pekola, Using materials for quasiparticle engineering, Mater. Quantum Technol. **2,** 013001 (2022).

[57] D. I. Schuster, A. Wallraff, A. Blais, L. Frunzio, R.-S. Huang, J. Majer, S. M. Girvin, and R. J. Schoelkopf, ac Stark Shift and Dephasing of a Superconducting Qubit Strongly Coupled to a Cavity Field, Phys. Rev. Lett. **94,** 123602 (2005).

[58] O. Astafiev, Yu. A. Pashkin, Y. Nakamura, T. Yamamoto, and J. S. Tsai, Quantum Noise in the Josephson Charge Qubit, Phys. Rev. Lett. **93,** 267007 (2004).

[59] Y. Hao, F. Rouxinol, and M. D. LaHaye, Development of a broadband reflective T-filter for voltage biasing high-*Q* superconducting microwave cavities, Appl. Phys. Lett. **105,** 222603 (2014).

[60] K. Funo, N. Lambert, B. Karimi, J. P. Pekola, Y. Masuyama, and F. Nori, Speeding up a quantum

refrigerator via counterdiabatic driving, Phys. Rev. B **100**, 035407 (2019).

[61] P. Menczel, T. Pyhäranta, C. Flindt, and K. Brandner, Two-stroke optimization scheme for mesoscopic refrigerators, Phys. Rev. B **99**, 224306 (2019).

[62] G. Schaller, S. Mostame, and R. Schützhold, General error estimate for adiabatic quantum computing, Phys. Rev. A **73**, 062307 (2006).

[63] D. M. Pozar, *Microwave Engineering* (Wiley, Hoboken, New Jersey, 2005), 3rd ed.